Taking control of charge transfer : strategic design for solar cells

Monti, Adriano

Chapter 3

Engineering a Donor-Antenna-Acceptor Triad for Photoinduced Charge Separation

3.0.ABSTRACT

In this chapter a series of donor-antenna-acceptor molecular rectifiers designed as modules for solar energy conversion devices are investigated via Density Functional Theory. We consider triad modules containing phenothiazine (PTZ) as electron donor and different derivatives of naphthalene diimide (NDI) as antenna and secondary electron acceptor. The choice of the molecular components in the triad is guided by the redox and optical properties of each subunit. Using time-dependent DFT in combination with the long-range corrected xc-functional CAM-B3LYP we investigate how photoinduced charge transfer states are affected by systematic modifications of the triad molecular structure. In particular, we show how by controlling the length of the molecular bridges connecting the different charge separator subunits it is possible to control the driving force for the evolution of the excitonic reactant state into the charge separated product state. Based on these findings we propose a supramolecular triad consisting of inexpensive and readily available molecular components that can find its implementation in artificial devices for solar energy transduction.

This chapter is based on the publication:

Monti, A.; de Groot, H.J.M.; Buda, F. In-Silico Design of a Donor–Antenna–Acceptor Supramolecular Complex for Photoinduced Charge Separation. *J. Phys. Chem. C* **2014**, *118*, 15600-15609.

3.1. INTRODUCTION

Progress in the design and synthesis of nanodevices for photovoltaics and artificial photosynthesis can be strongly supported by computational modeling methods able to predict optimal target properties for light energy conversion in the computer prior to the realization in chemical laboratories[1,22,3,4,5].

In the past decades, the efficiency of photovoltaic and photochemical systems has been significantly improved. A clear example is represented by the power conversion efficiency of dye-sensitized solar cells, which has been increasing from the 7% of the first cell proposed by O' Regan and Grätzel, to the current value of 20% of perovskite based systems[6,7]. Despite these results, optimization of these devices for solar energy conversion is far from being achieved.

As explain in chapter 1, these systems are often composed of a molecular or solid-state chromophore coupled to a wide band-gap semiconductor. The chromophore photoabsorption induces the formation of an exciton reactant state. This is then dissociated as the excited electron is injected into the semiconductor conduction band, to form the charge separated product state. The collected electron can then be used to perform work or generating solar fuel. The positive hole left on the oxidized chromophore is quenched by means of a sacrificial reducing agent, or through water oxidation catalysis. The solar energy stored by photoexciting the chromophore may be lost if the system recombines to its ground state before the product state can be stabilized by driving the hole and the electron apart.

This undesired process, which can severely hamper the energy conversion efficiency of a devices, takes the name of charge recombination or back electron transfer. Recombination to the ground state can occur directly from the excitonic state or, if an electron is trapped at the semiconductor surface, even after the electron injection has occurred.

In natural systems, back electron transfer is prevented by quickly spatially separating the electron and the hole generated upon photoexcitation. This is achieved through a series of redox reactions between consecutive compounds with increasingly lower redox-potentials. It is observed that the charge recombination rate decays exponentially with the distance between the electron donor and acceptor units[8,9].

Through the electron transport chain depicted in **Scheme 3.1a**, the excited electron is transferred from the electron donor pigment $P680^{*}$ in PSII to the pigment P700 in PSI. The $P680^{+\cdot}$ is then reduced by a tyrosine residue (Tyr) in PSII, which is later reduced by the water oxidation catalyst.

In PSI, the photoexcitation of P700 initiates a secondary electron transfer cascade culminating in NADPH production (see **Scheme 3.1a**).

The transfer of the photoexcited electron from P680* to the quinone Q_A occurs on a sub-nanosecond time scale preventing the slower exciton recombination to the ground state. Additionally, once the excited electron reaches Q_A, its distance from $P680^{+\cdot}$ becomes too large to allow the recombination of the charges.

The number of subunits employed by the natural photosynthetic system to achieve the electron/hole charge separation, is however too large to be efficiently reproduced in an artificial device. A different design strategy is needed that requires a smaller number of subunits while still avoiding charge recombination events.

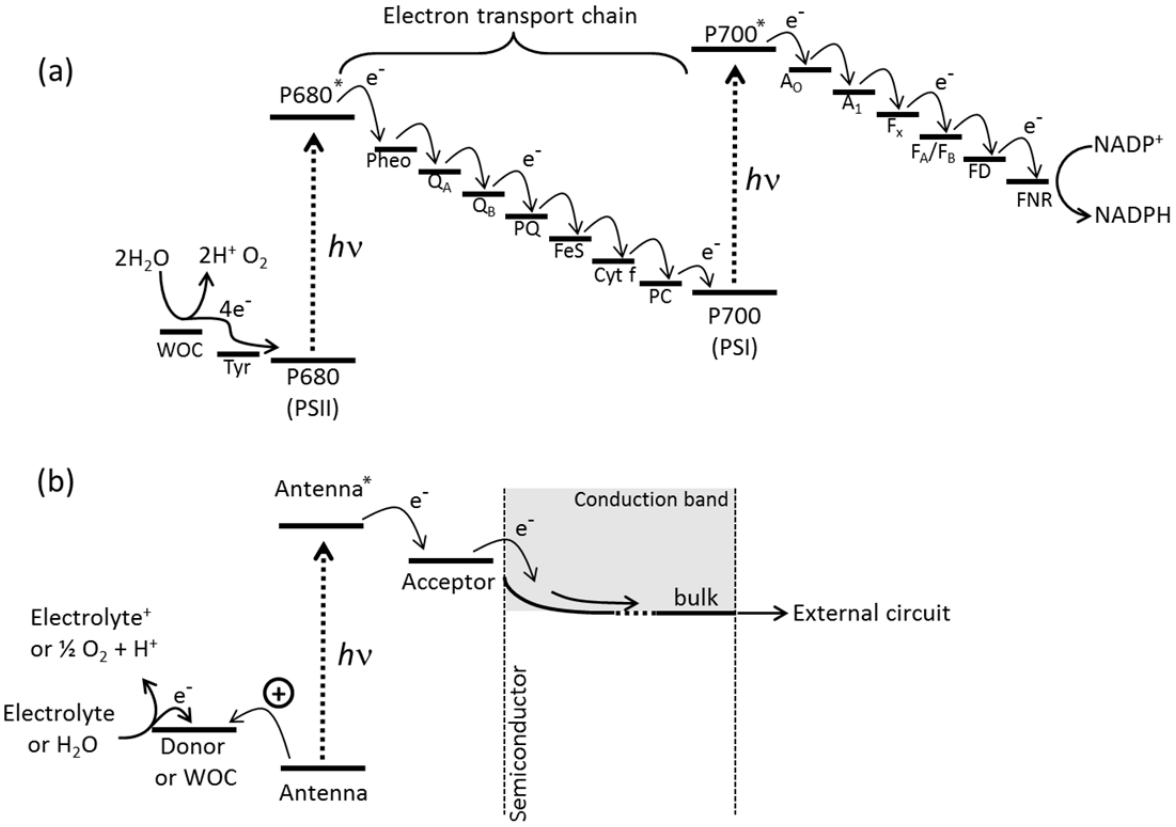

Scheme 3.1. (a) Schematic energy diagram of the natural photosynthesis mechanisms driven by the photoabsorption of the chromophore pigments P680 and P700, leading to electron flowing between the water oxidation catalyst (WOC) and the ferredoxin-$NADP^+$ reductase (FNR). This representation, readapted from references [10,11], takes the name of Z-scheme. (b) Schematic energy diagram of a donor-antenna-acceptor triad applied as photosensitizer at the anode of a photovoltaic or photochemical cell.

Recent publications suggest that the recurrence of charge recombination in photochemical and photovoltaic devices can be reduced through systems composed of three or more subunits arranged in a Donor-Antenna-Acceptor (D-An-A) like design, presenting an optimized energy gradient and electronic coupling[12,13,14,15]. In this type of structures, upon photoexcitation of the antenna module, the charge

separation is achieved by transferring the electron and the hole in opposite directions. As shown in **Scheme 3.1b**, upon its formation, the exciton localized on the antenna is dissociated through two charge transfer processes: (i) transfer of the excited electron from the chromophore to the acceptor; (ii) reduction of the antenna through hole transfer onto the donor water oxidation catalyst (WOC), which becomes the oxidized species. The presence of the antenna complex between the donor and the acceptor should induce a considerable tunneling barrier for charge recombination and consequently reduce the electronic coupling between the charge separated and ground states of the triad. Like in the natural system, this will result in delaying the electronic recombination to the state of minimal energy and increase the lifetime of the charge separation for a time sufficient for redox reactions to occur at the donor and acceptor sites. In fact, within a photoanode for solar cell devices, these type of triads are bound directly to the surface of a suitable semiconductor through the acceptor unit. After formation of the charge separated state, electron injection can occur from the acceptor into the semiconductor, while the oxidized donor can be reduced to its neutral form by a sacrificial reductant, or through water oxidation (**Scheme 3.1b**). The regenerated triad can thus absorb another photon and reinitiate the cycle. If an electron is trapped at the semiconductor surface, it may quench the excitonic state induced by the second photon. The presence of the electron acceptor between the antenna and the semiconductor is meant to prevent this recombination by introducing a barrier for the back electron transfer.

In this chapter we show how Density Functional Theory (DFT) based methods can be used to optimize the optical and electronic properties of a molecular system designed for photovoltaics and photoelectrochemical applications prior to its experimental realization. The aim is to design a photosensitive triad-like charge separator which shows ultrafast unidirectional electron transfer leading to the formation of a charge separated state (CS) sufficiently stable to kinetically allow redox reactions at the donor (D) and the acceptor (A) moieties[16]. We choose the triad components on the basis of their ground and excited state redox potentials in order to obtain negative potential energy gradients between the donor-antenna and the antenna-acceptor subunits. Furthermore, the donor and the acceptor are chosen considering the potential boundaries necessary to couple the proposed triad within a device employing a silicon electrode and a commonly used electrolyte, such as iodide/triiodide.[17]

Through systematic changes in the linkage between the donor, the antenna and the acceptor, it is highlighted how structural modifications can be used to control the relative energies and electronic couplings between different excited states. In this way we are able to design a molecular triad for which the photoexcitation of the

antenna will trigger redox processes resulting into the formation of a final D^+-An-A^- charge separated state. The molecular components used in this study as donor, antenna, and acceptor are respectively the 10,10a-dihydro-4aH-phenothiazine (PTZ), the 2,6-diethoxy-1,4,5,8-diimidenaphthalene (NDI_1), and the 2,6-dicarbonitrile -1,4,5,8-diimidenaphthalene (NDI_2). A schematic representation of the single components and of the different complexes analyzed is reported in **Figure 3.1**.

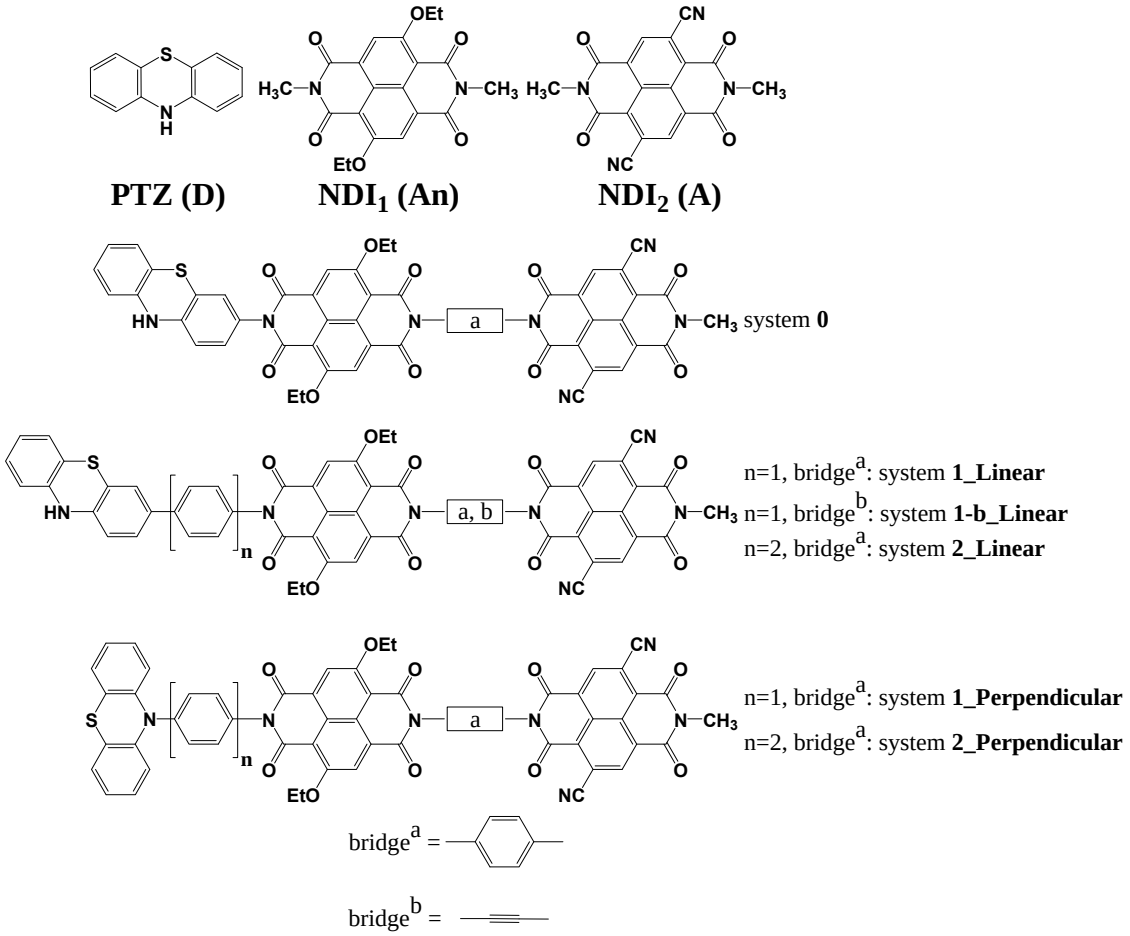

Figure 3.1. Molecular structures of the studied compounds. PTZ acts as electron donor (D), NDI_1 as antenna (An) and NDI_2 as electron acceptor (A). The number of phenyl units between D and An is indicated with n. Two different bridges (a and b) between An and A are considered. Linear and Perpendicular refer to the relative arrangements of PTZ and the phenyl bridge.

Individually, PTZ, NDI_1 and NDI_2 have already been discussed in the literature and are well known for their robustness and ease of synthesis. They have been chosen based on the perfect match between their well-characterized optical and electronic properties and the device requirements. The members of the naphthalene diimide family form an important class of chromophores which has been extensively analyzed in recent years and applied in a wide range of devices, such as

supramolecular switches, chemosensors, n-type semiconductor in organic transistors, light-harvesting chromophores in dye-sensitized solar cell (DSSC), and as electron acceptor in photoactivated artificial charge separators[18–20,21,22]. The versatility of these compounds is due to their peculiar electronic properties that can be easily tuned through a selective functionalization of the naphthalene core[23]. By choosing the appropriate functional groups it is possible to adjust the HOMOs and LUMOs orbital energies and their relative gaps. This allows to control the molecular absorption range and to adapt the molecular redox properties with respect to the environment requirements.

As shown by Sakai et al[23] due to their different functionalization NDI_1 and NDI_2 present absorptions in two different regions of the incoming photon spectrum. While the first is photoactive also into the visible, the second shows activity only in the UV-region. This ensures NDI_1 to be the only active chromophore for applications with visible light in solar energy conversion. On the other hand, NDI_2 is chosen not only for its absorption properties but also for its characteristic ability to form stable anionic radicals.[24] Especially in a context where several molecules are bound together through $\pi-\pi$ stacking, NDI_2 has been shown to behave as a n-type semiconductor material.[25] This characteristic makes it a very good candidate as electron acceptor able to increase the electron-hole distance through electron delocalization, thus decreasing the probability of its recombination into the ground state. Additionally, the LUMO energy of NDI_2 aligns well with the valence band of silicon, opening the possibility of establishing a p-n junction between the electron rectifier and a silicon-based electrode.

Finally, phenothiazine is a strong reducing agent photoactive only in the UV-region that is already widely employed as pesticide and in pharmaceutical or optical applications[24,26,27]. Thanks to the strong interaction between the $2p_z$ electrons of the nitrogen atom of the central heterocyclic ring with the peripheral benzenes, PTZ can easily form cation-radical species and stabilize them through resonance delocalization of the positive charge into those electron-rich moieties[26]. PTZ is therefore an optimal electron donor able to quench the hole created into the antenna upon photoexcitation.

Herein we compare a series of molecular triads designed for photoinduced unidirectional charge separation. The Donor-Antenna distance proves to be a key parameter to control the relative energies of different excited states potential energy surfaces (PES). It is shown that it is possible to induce the concerted hole/electron transfer mechanism as dominant path for the formation of the charge separated state D^+-An-A^-, while avoiding the unwanted partially separated intermediate state D^+-An^--A (see **scheme 3.2**). Geometrical and structural modifications are applied to

the bridge units to find an optimal balance between thermodynamics and electronic coupling requirements for a fast unidirectional charge transfer. The results lead to the design of the triad **1-b_Linear** (**Figure 3.1**, third panel from top), for which ultrafast charge separation is predicted.

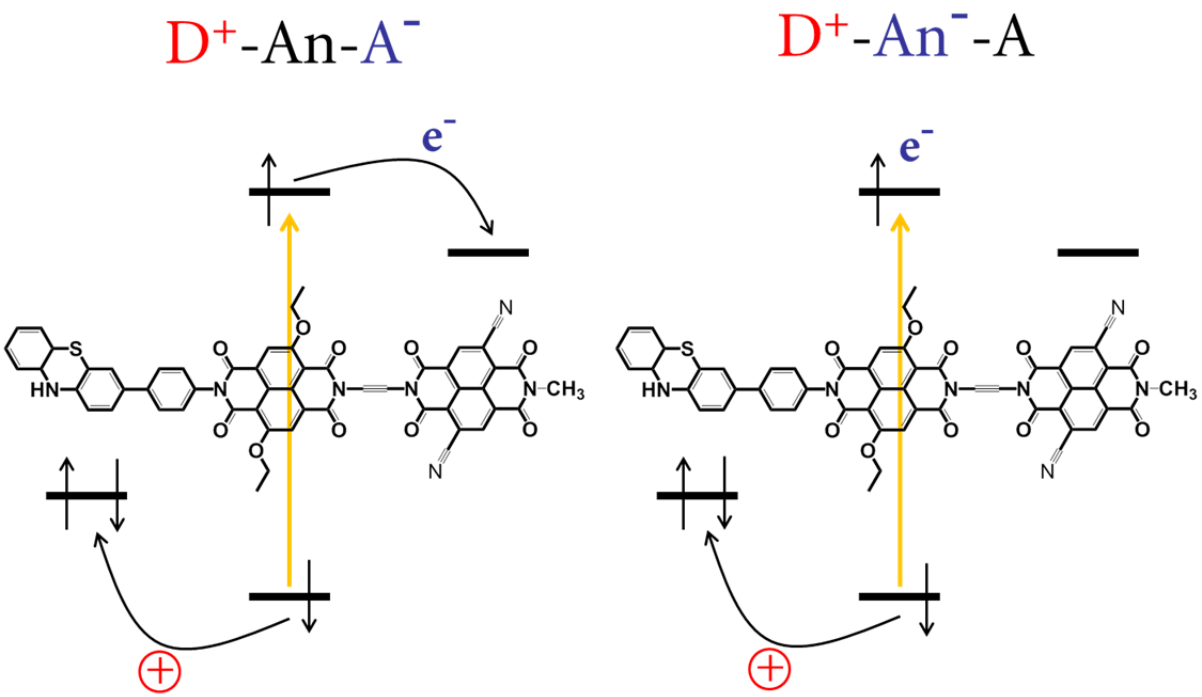

Scheme 3.2. Schematic energy diagram of the frontier molecular orbitals involved in the charge transfer processes leading to the formation of the charge separated (D^+-An-A^-, left) and intermediate state (D^+-An^--A, right). The yellow arrow represents the photoexcitation of the antenna, while the curved arrows show the direction of the electron (e^-) and hole (+) transfer.

3.2. METHODS AND COMPUTATIONAL DETAILS

3.2.1. Ground State calculations

To optimize the ground state geometries of each monomer, dyad and triad presented in this work we make use of the ADF software package[28–30]. The geometries are optimized at the B3LYP[53]/TZP level of theory in a dichloromethane (DCM) environment described by the continuum solvent model COSMO[31]. Van der Waals dispersion interactions are included using the Grimme3-BJDAMP correction.[32]

3.2.2. Time-Dependent DFT

Time-Dependent DFT (TD-DFT) is used to calculate the absorption spectra of the investigated systems and to check how the optical properties of the singular components are affected by the assembling into the triad complexes. Several exchange-correlation functionals available in the ADF computational package have

been used to check the accuracy of our results against available experimental data (see results and discussion section 3.3.1).

3.2.3. Ground and excited state redox potentials

ADF is used for the calculation of the ground and excited state oxidation potentials of the donor, antenna and acceptor monomers. Following the procedure described by De Angelis et al[33], the ground state oxidation potential is estimated as

$$G_{ox}^{GS} = G_{sol}^{0} - G_{sol}^{+} \quad (3.1)$$

Both G_{sol}^{0} and G_{sol}^{+} are obtained by adding the solvent effect to the energies of the molecules optimized in vacuum. The solvent contribution is estimated as the energy difference between the system in solution and in vacuum, calculated at the geometry optimized in solution.

The excited state oxidation potential G_{ox}^{ES} is obtained by subtracting from G_{ox}^{GS} the adiabatic lowest transition energy (E_{0-0}):

$$G_{ox}^{ES} = G_{ox}^{GS} - E_{0-0} \quad (3.2)$$

where E_{0-0} is the energy difference between the excited and the ground states at their corresponding optimized geometries. Results were validated also by calculating the ground state oxidation potentials using the ΔSCF and Born-Haber cycle methods[34]. All methods can reproduce the experimental redox values with an error <0.1 eV.

3.2.4. Excited state geometry optimizations

To investigate the possible electronic relaxations that can occur after photoabsorption, we optimize, for each charge separator, the (i) excitonic state, denoted throughout this chapter as S0, in which both hole and electron are localized on the antenna; (ii) the full charge separated state S1 in which the hole is on the donor and the electron on the acceptor; and (iii) the intermediate CS state S2 in which only the hole moves on the donor and the electron stays on the antenna. Other excited states have been investigated but they all turned out to be much higher in energy, indicating that their formation is strongly unlikely upon visible light absorption. For each complex, starting from their ground state optimized geometry, we initially induce a specific optical transition from the ground state to the diabatic state of interest and subsequently we optimize the geometry of such an excited state. In order to overcome the systematic underestimation of the excitation

energies associated with strong molecular charge transfer character shown by most *xc*-functional[35], we make use of the long-range corrected functional CAM-B3LYP[36], which has been shown to be quite accurate in describing electronic excitations with strong charge transfer character[37,38]. At the same time this functional is reasonably accurate in estimating the energy of excitation with strong excitonic character. These calculations are performed using the Gaussian 09 program package[39] using the cc-pVDZ basis set and the Polarizable Continuum Model to simulate the DCM solvation[40].

3.2.5. Electronic coupling calculations

To avoid confusion with the use of the terms donor and acceptor recurring in other sections, we need to specify that when describing hole-transfer processes, with the term donor we refer to the phenothiazine subunit, while with acceptor to the antenna NDI_1. On the other hand, for the electron transfer calculations the terms donor and acceptor have to be intended as the subunits NDI_1 and NDI_2, respectively.

The coupling strength between the orbitals involved in the hole/electron transfer processes are estimated using both the charge transfer integrals (CTI) method implemented in ADF[41–43], and the Constrained DFT (CDFT) computational scheme[44–46] implemented in the software package CPMD[47].

3.2.5.1. Charge transfer integral (CTI) method

This formalism computes the CTI through the equation:

$$H_{\mathrm{DA}}^{\mathrm{CTI}} = J_{\mathrm{DA}} - \frac{1}{2} S_{\mathrm{DA}}(e_{\mathrm{D}} + e_{\mathrm{A}}) \tag{3.3}$$

Here, J_{DA} represents the off-diagonal elements of the Fock matrix constructed using the HOMOs (for hole transfer calculations) or the LUMOs (for electron transfer) of the molecular subunits used as donor (D) or acceptor (A). S_{DA} is the overlap integral between the molecular orbitals of the two states considered, while e_{D} and e_{A} are the energies of the system bearing the electron/hole on the donor or the acceptor. These calculations are performed at the B3LYP/TZP level in dichloromethane simulated through the continuum solvation model COSMO.

3.2.5.2. Constrained DFT (CDFT)

This methodology is based on the idea of minimizing the Kohn-Sham energy functional under the constraint that the charge difference between two defined regions of space is equal to a specific value of interest (see section 2.6 of this thesis). Within the CPMD implementation, we can define these two regions of space

as the sum of the atoms constituting respectively the donor and the acceptor. For the process of hole-transfer, we consider the sub-system PTZ-phenyl-NDI_1 in its linear configuration. Here, PTZ and the phenyl bridge (Ph) form the donor, while NDI_1 is the acceptor. The electronic coupling is calculated between the two states donor$^+$-acceptor and donor-acceptor$^+$. Similarly, the electron coupling between NDI_1 and NDI_2 is estimated as the coupling between the two states NDI_1^--bridge-NDI_2 and NDI_1-bridge-NDI_2^-. For the bridge unit we consider either a phenyl ring, or an ethyne group; in this case the bridge is not included neither in the definition of donor nor in that of the acceptor. The CDFT calculations are performed in vacuum using the pseudopotentials of ref. [48] with a plane wave cut-off of 70 Rydberg.

3.2.6. Bridge-mediated electron transfer

Depending on the structure of the triad considered, the process of hole-transfer can take place directly between donor and acceptor, or can proceed via bridge-mediated tunneling mechanism. In contrast, the electronic relaxation from NDI_1 to NDI_2 occurs as bridge-mediated electron tunneling for every system investigated. For those cases in which the charge transfer occurs through bridge-mediated tunneling, and the donor and acceptor are separated by M identical bridge units, the overall donor-acceptor electronic coupling is calculated following the McConnel's formalism[49]:

$$H_{\mathrm{DA}}^{\mathrm{BM}} = \frac{h_{\mathrm{Db}}}{\Delta\varepsilon}\left(\frac{h_{\mathrm{bb}}}{\Delta\varepsilon}\right)^{M-1} h_{\mathrm{bA}} \qquad (3.4)$$

In equation 3.4, h_{Db}, h_{bA} and h_{bb} represent the coupling between a bridge unit and respectively the donor, the acceptor and another bridge unit (if present). These terms are calculated using both the CTI or the CDFT methods.

The other parameter, $\Delta\varepsilon$, represents either the hole, or the electron tunneling energy gap imposed by the bridge (**Scheme 3.3**). The height of the hole tunneling barrier ($\Delta\varepsilon_{\mathrm{hole}}$) is calculated as the difference between the HOMO energy values of the antenna and the bridge1 interposed between donor and antenna.

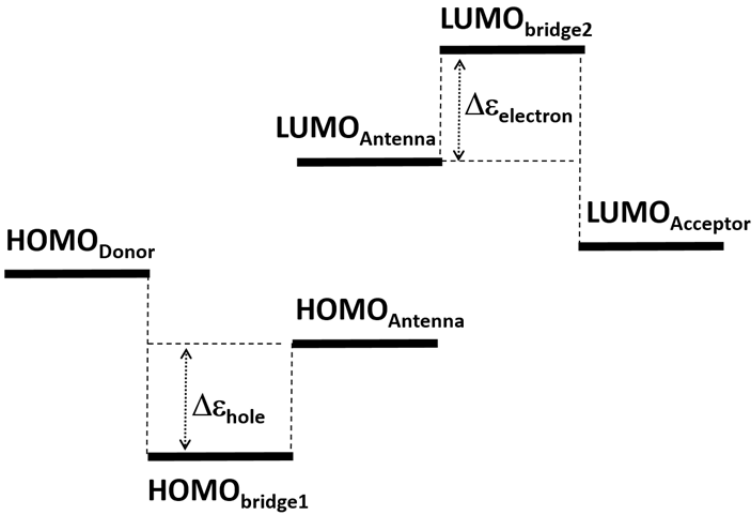

Scheme 3.3. Energy diagram of the Donor-Antenna-Acceptor orbitals used to calculate the energy barriers for the hole and electron tunneling, to be used in equation 3.4.

In contrast, for the electron tunneling, $\Delta\varepsilon_{\text{electron}}$ is calculated as the energy difference between the LUMOs of the antenna and of bridge2, interposed between the antenna and the acceptor. It has been verified that this method provides values of $\Delta\varepsilon$ very similar to those calculated with the computationally more expensive CDFT method by constraining the charge over the bridge.

Equation 3.4 is the generalized form of the McConnel's formalism, where M>0. Since in this chapter the electronic coupling is calculated only for systems in which M=1, the second term on the right hand side of equation 3.4 becomes equal to 1. This formalism is applied only to the calculation of the coupling between states which are not delocalized over bridge units.

3.3. RESULTS AND DISCUSSION

We initially present in section 3.3.1 the results of the TD-DFT analysis performed on a series of molecules used as benchmark to assess the quality of the results given by different GGA and hybrid *xc*-functionals, in reproducing the experimental absorption spectra published by Matile et al[23,50]. This analysis is useful to understand the level of theory required to accurately describe the optical response of the investigated triads to their initial photoexcitation.

An accurate calculation of the ground and excited state oxidation potentials of the chosen molecular subunits is essential to verify that the donor, antenna and acceptor moieties do indeed create the redox gradient required for the unidirectional charge transfer. In section 3.3.2 we compare the computed redox values obtained using the method described in section 3.2.3, with the experimental cyclic voltammetry data[19].

In section 3.3.3 and 3.3.4 we extend the TD-DFT study of molecular optical properties to a set of triads on which we apply specific structural changes. We study how these modifications affect the energetics of each excited state by TD-DFT geometry optimization. Starting from the systems showing the most promising thermodynamics we further modify the molecular structure in order to optimize also the electron-coupling between donor, antenna and acceptor. Finally, for the optimized molecular rectifier we estimate the charge separation rate constant.

3.3.1. xc-functional benchmarking for TD-DFT absorption spectra

TD-DFT studies are performed on the benchmark compounds NDI_1, NDI_2 and NDI_0[16,22,23] making use of the exchange-correlation (xc) functionals OPBE[51], SAOP[52,53], OPBE0[54], B3LYP[55] and M06[56,57].

In **Table 3.1** we compare the calculated and the experimental values of the first characteristic absorption peak of each molecule investigated.

Table 3.1. Excitation energies analysis of the reference compounds NDI_0, NDI_1, NDI_2 performed with TD-DFT and various *xc*-functionals. The experimental value is also reported for comparison.

		[a] HF_x	[b] transition	[c] f	[d] λ_{abs}(nm)	[e] E_g(eV)
NDI_0						
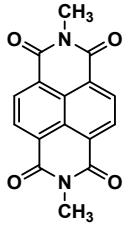	OPBE	0%	**H → L (98%)**	0.46	433	2.86
	SAOP	0%	**H → L (98%)**	0.47	443	2.80
	B3LYP	20%	**H → L (99%)**	0.59	409	3.04
	OPBE0	25%	**H → L (99%)**	0.61	391	3.17
	M06	25%	**H → L (98%)**	0.61	390	3.17
	Exp.				380	3.26
NDI_1						
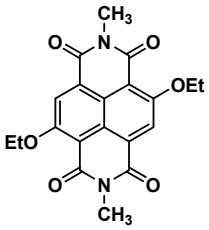	OPBE	0%	**H → L (97%)**	0.31	561	2.21
	SAOP	0%	**H → L (98%)**	0.30	539	2.30
	B3LYP	20%	**H → L (99%)**	0.42	482	2.54
	OPBE0	25%	**H → L (98%)**	0.43	466	2.66
	M06	25%	**H → L (99%)**	0.43	474	2.62
	Exp.				470	2.63
NDI_2						
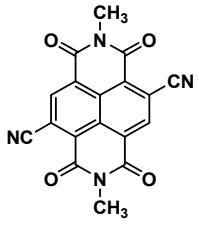	B3LYP	20%	**H → L (97%)**	0.47	424	2.92
	OPBE0	25%	**H → L (99%)**	0.49	406	3.05
	M06	25%	**H → L (99%)**	0.48	411	3.01
	Exp.				380	3.26

[a] Amount of exact *HF*-exchange for each functional. [b] Main molecular orbital transition (relative percentage) associated to electronic excitation $\mathbf{E_g}$. [c] Oscillator strength. [d] Maximum absorption wavelength corresponding to the computed electronic excitation energy. [e] Electronic excitation energy computed in methanol. Experimental values in methanol are adapted from references [22] and [23].

These results clearly indicate that hybrid and meta-hybrid functionals (B3LYP, OPBE0, and M06) are able to predict the lowest excitation energies of the benchmark molecules with much higher accuracy compared to the GGA functional OPBE[51] and the model potential SAOP[52,53], which considerably underestimate the experimental values.

3.3.2. Redox potential calculations

To verify the presence of a potential gradient between the donor, the antenna and the acceptor suitable to induce charge separation, we compute the ground and excited state redox potentials of each subunit following the procedure described in section 3.2.3. As shown in **Table 3.2**, the redox values calculated at the B3LYP/DCM (COSMO) level compare well with the experimental cyclic voltammetry onset values[22,23,26]. These results overall confirm the validity of the applied method and computational set up. Considering also the positive results obtained with TD-DFT (B3LYP reproduces the NDI_1 excitation energy within 0.1 eV from the experiment), the choice of the hybrid B3LYP functional appears to be appropriate for studying the electronic and optical properties of molecular complexes employing these functional subunits.

Table 3.2. Ground (ΔG_{ox}) and excited state (ΔG_{ox}^{ES}) molecular redox potentials estimated for each molecular component of the triad.

Molecule	Redox Pot.	[a]E_{exp}(eV)	[b]E_{calc}(eV)
NDI_1	ΔG_{ox}	-6.16[22]	-6.21
	ΔG_{ox}^{ES}	-3.82[22]	-3.68
NDI_2	ΔG_{ox}	-7.50[23]	-7.53
	ΔG_{ox}^{ES}	-4.50[23]	-4.60
PTZ	ΔG_{ox}	-4.77[26]	-4.86

[a] Experimental onset redox potentials (measured in dichloromethane). [b] Redox potential values computed using B3LYP *xc*-functional in DCM (COSMO) model. All data are reported vs. vacuum.

3.3.3. Optical excitations and excited state geometrical optimizations

The electronic structure of system **0** (see **Figure 3.1**) is obtained at the ground state geometry after optimization in dichloromethane, for consistency with the redox potentials calculations. The frontier orbitals are depicted in **Figure 3.2**.

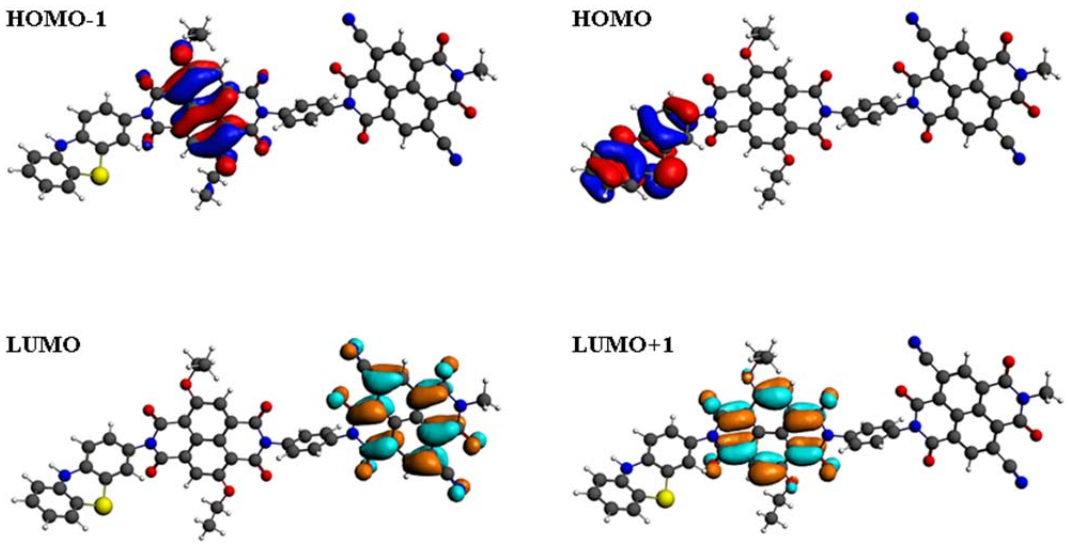

Figure 3.2. Frontier molecular orbitals of triad **0** obtained at the B3LYP/TZP level of theory in DCM solvent.

As expected from the ground and excited state oxidation potential calculations, the HOMO and the LUMO are highly localized on the donor and the acceptor respectively, while the HOMO-1 and the LUMO+1 reside on the antenna. Each of these four orbitals possesses the same symmetry of those involved in the main excitation of the subunits calculated separately. The absorption spectrum calculated for system **0** (**Figure 3.3**, black line) shows a dominant peak around 500 nm, corresponding to the photoinitiated HOMO-1 to LUMO+1 transition. **Figure 3.3** shows for comparison also the spectra computed for the monomers NDI_1 and NDI_2, respectively in blue and red dotted lines. The most noticeable difference between these spectra is represented by a 18 nm (0.04 eV) red shift of the first absorption peak of triad **0** with respect to that of the isolated NDI_1. Similar shifts are observed for the absorption spectra estimated using the *xc*-functionals OPBE0 (0.08 eV) and OPBE (0.07 eV). This red-shift reveals the influence of the substituents coupled to the imide groups on the transition energy of the antenna.

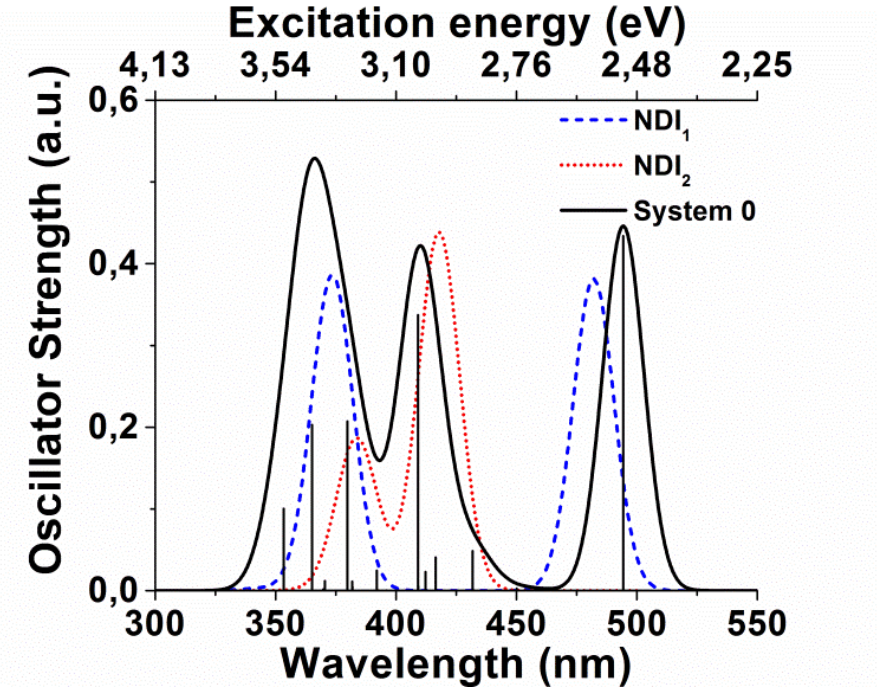

Figure 3.3. Optical absorption spectra computed with TD-DFT/B3LYP for NDI_1 (blue dashes), NDI_2 (red dots), and for the whole triad system **0** (black curve). The black solid lines represent the calculated excitations contributing to the absorption spectra of system **0**. TD-DFT calculations are performed in DCM (COSMO) using the TZP basis set, within ADF.

The differences between the excited states oxidation potentials of NDI_1 and NDI_2, as well as between the ground states potentials of PTZ and NDI_1 (**Table 3.2**), imply the presence of driving forces across the linking motifs that represent tunneling barriers separating the components of the triad. Consequently, photoexcitation of the antenna creates the conditions for the exothermic formation of a full charge separated state where the photogenerated positive hole and the excited electron are localized respectively on the donor and the acceptor.

To investigate how structural changes can influence the probability of formation of different excited states after photoabsorption, we performed TD-DFT geometry optimizations in the electronic states S0, S1 and S2, for each of the aforementioned systems. The geometrical parameters of the systems optimized for different excited states are summarized in **Table A3.1** in the appendix. For all the investigated cases we observe that in its neutral state, the phenothiazine is bent around the N-S axis with an angle of ~146.8° while, after oxidation (excited states S1 and S2), the molecule assumes a fully planar configuration. This indicates that this particular degree of freedom can be associated with the process of charge transfer between donor and antenna. Moreover, we observe that the dihedral angle between the PTZ and the directly bound phenyl bridge assumes different values depending on the

configuration of PTZ. When the PTZ is in a perpendicular configuration (see **Figure 3.1**) this angle is close to 90°, while for PTZ in the linear configuration it is found to be ~36°, which is consistent with previously studied systems containing phenyl bridges[58]. The variation of this torsional angle has an important effect on the conjugation of donor and bridge units, and thus on the relative stability of different excited states.

We also observe that optimization in S0 does not lead to any major geometrical change compared to the ground state, independently of the rectifier considered. The maximum energy difference evaluated at the ground state PES between the geometries optimized in the ground and the excitonic states is ~0.01 eV. This is at least one order of magnitude smaller than the difference calculated for the geometries optimized in any other excited state. The energy minimum of S0 is used as reference point to appreciate how the energies of S1 and S2 are affected by structural modifications.

In the context of the Marcus theory of electron transfer, the excitonic state S0, populated upon photoexcitation, is considered as the reactant state and the fully charge separated state S1 as the product state. In contrast, the intermediate state S2 represents an unwanted product state and its formation has to be avoided (see **Scheme 3.2**). Within this framework, the energy difference between the minima of the reactant and each of the product states (ΔE), is considered the driving force for the corresponding electron transfer reactions.

To calculate the exact thermodynamic driving force, the energies of the system optimized in S0, S1 and S2, should be corrected for the entropic term. An explicit calculation of this term, however, becomes computationally too demanding for such extended systems.

For large molecular triads similar to the ones investigated here, it has been argued that the entropic term TΔS represents a minor correction to the free energy difference, compared to ΔE between optimized excited states[33,59]. Thus, in the following analysis the entropic contributions are neglected, leading to the approximation $\Delta E \approx \Delta G$. Hence, the term ΔG is used to indicate the energy difference (or driving force) between the minima of the optimized excited states.

Figure 3.4 and **Table 3.3** show the comparison between the PESs obtained through excited states geometry optimizations of the different charge separators.

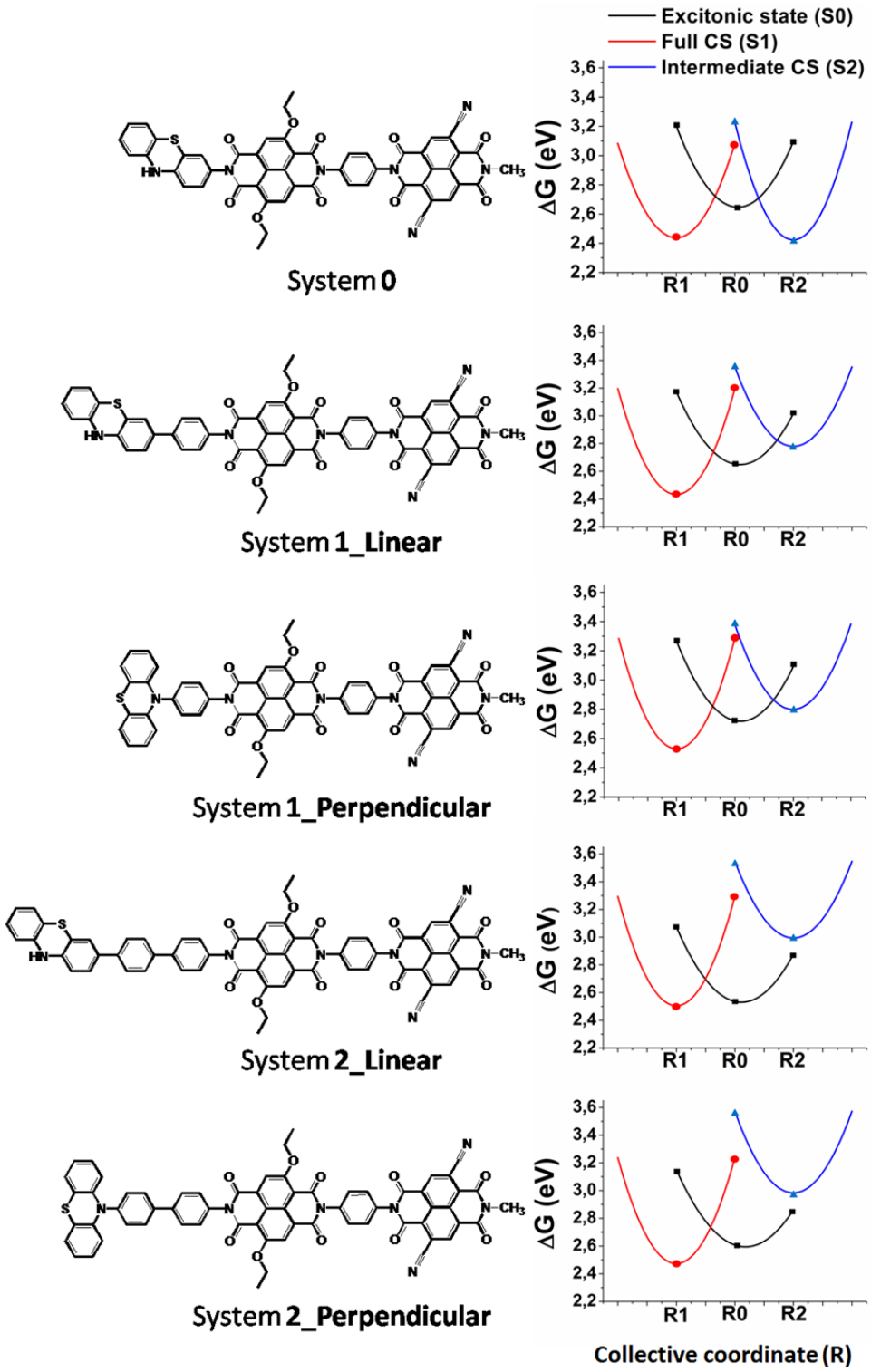

Figure 3.4. Potential energy surfaces for the antenna-localized exciton state S0 (black), the fully charge separated state S1 (red), and the intermediate charge separated state S2, representing the hole displacement from An to D (blue). The energies are obtained with TD-DFT geometry optimizations at the CAM-B3LYP/cc-pVDZ level and reported relative to the minimal energy of the ground state along a nuclear collective coordinate R. R0, R1 and R2 represent the geometries optimized for each excited state (**Table A3.1** in the appendix). The symbols along the curves represent the energy values used to construct the parabolas and calculate the reorganization energies λ and the energy differences between the excited states S0, S1 and S2 reported in **Table 3.3**.

Table 3.3. Minimal energy differences **ΔG** between excited state PES and reorganization energies **λ** calculated for the investigated systems.

	S1–S0		**S2-S0**		**S1-S2**	
	ΔG (eV)	**λ (eV)**	**ΔG (eV)**	**λ (eV)**	**ΔG (eV)**	**λ (eV)**
System **0**	-0.21	0.65	-0.22	0.80	0.014	0.41
System **1 Linear**	-0.22	0.76	0.13	0.57	-0.35	0.40
System **1 Perpendicular**	-0.19	0.75	0.08	0.58	-0.27	0.38
System **2 Linear**	-0.031	0.79	0.46	0.55	-0.49	0.39
System **2 Perpendicular**	-0.13	0.76	0.38	0.59	-0.51	0.50

ΔG values are calculated as the energy difference between the minima of the different excited state PESs (S_n-S_m) obtained through TD-DFT geometry optimization at the CAM-B3LYP/cc-pVDZ level of theory. λ is the reorganization energy calculated along the potential energy surfaces.

The first thing to notice in **Table 3.3** and **Figure 3.4** is that for system **0** the reactant state S0 is energetically higher than the two nearly degenerate product states S1 and S2. This implies that both states can be energetically accessed from S0, and that the driving forces are equal for the formation of either one of them.

The insertion of a phenyl bridge between PTZ and NDI_1 has a destabilizing effect for the intermediate state S2, both in the linear and perpendicular triads (system **1_Linear** and system **1_Perperpendicular** in **Figure 3.4**). This effect is further enhanced by adding a second phenyl bridge (see system **2_Linear** and system **2_Perperpendicular** in **Figure 3.4**). The results summarized in **Table 3.3** show a linear dependence of ΔG (S2-S0) on the donor-antenna distance ($R_{D\text{-}An}$). In particular, it is found that the destabilization of S2 is linearly dependent on the number of bridge units introduced, with each ring corresponding to $R_{D\text{-}An}$ increasing by ≈4.3 Å. The destabilization per ring is equivalent to 0.35 eV for the linear systems, and to 0.30 eV for the perpendicular ones. This observation is relevant to design a system in which the formation of the unwanted product state S2 can be avoided in favor of S1.

The energy of the S1 minimum does not significantly change for systems with different bridge lengths (**Figure 3.4**). However, **Table 3.3** shows that the insertion of a first phenyl ring between donor and antenna only marginally affects ΔG (S1-S0), while the insertion of a second ring significantly reduces the thermodynamic force with respect to the excitonic state, especially for the linear case. This effect appears to be induced mostly by a shift of the energy minimum of S0.

Overall, these results indicate system **1** as the best design choice for the optimization of the driving force towards the full charge separated state. The use of a phenyl bridge to seprate the antenna from both the donor and the acceptor, favors the transition between the reactant state S0 to the product state S1. At the same time, it destabilizes the intermediate state S2 with respect to S0, in such a way that

a spontaneous transition between them is impossible.

Thus, the S1 state is expected to be formed by a concerted transfer of an hole from the antenna to the donor and an electron from the antenna towards the acceptor (see **Scheme 3.2**). In the following section 3.3.4 the reasons for a preference between the perpendicular or the linear geometry for system **1** are discussed.

3.3.4. Charge transfer integrals and charge separation rates

So far our analysis has been focused on the effects that structural changes have on the energy gradients between different excited states. However, in order to assess the charge separation efficiency of a particular triad we cannot limit our analysis solely to the system's thermodynamics. Indeed, although Marcus[60] theory (see section 1.4) defines the electron-transfer rate constant (k_{ET}, equation 3.5) between two electronic states as directly dependent on their energy difference (ΔG) and the reorganization energy (λ),

$$k_{\mathrm{ET}} = \frac{2\pi}{\hbar}\frac{2}{\sqrt{4\pi\lambda k_B T}}|H_{\mathrm{DA}}|^2 \exp\left(-\frac{(\Delta G+\lambda)^2}{4\lambda k_B T}\right) \qquad (3.5)$$

the probability of this process to occur is strictly correlated also to the electron coupling term (H_{DA}), which relates to the degree of mixing between those two electronic states.

As it will be shown in chapter 4, coherent electron-nuclear motion can have crucial effects on electron tunneling processes since it can drive the system towards the crossing point of the initial and final states, where the electron transfer takes place.

Table 3.4 summarizes the electronic coupling between the different subunits calculated for both the linear and perpendicular system **1** using both the CTI and CDFT methods.

The orbital analysis of system **1** in its linear and perpendicular geometries show highly localized frontier molecular orbitals that strongly resemble those already discussed for system **0**. The only difference is represented by the HOMO of system **1_Linear**, which appears to be delocalized over both the PTZ and the phenyl bridge. This indicates that the bridge does no longer constitute a barrier in the process of hole-transfer between the antenna and the electron donor, but instead it is a part of the donor group.

This delocalization is no longer observed in system **1_perpendicular**, where the phenyl bridge acts as barrier for the transfer. The energy difference between the

HOMO of the antenna and the first occupied orbital localized on the bridge, is much smaller than the energy difference between the HOMO of the donor and LUMO of the bridge. The charge transfer between donor and antenna is therefore expected to occur primarily as a hole rather than as an electron transfer process, since the tunneling barrier imposed by the bridge is considerably smaller for the first process[61].

The delocalization of the LUMO or the LUMO+1 over the bridge in between the antenna and the acceptor is never observed for any of the investigated systems. The electron transfer between antenna and acceptor thus proceeds via electron tunneling through the bridge.

To calculate the coupling between the electronic states involved in the formation of the charge separated state S1, the donor-bridge-antenna and antenna-bridge-acceptor subsystems, listed in **Table 3.4** (first column), are studied separately. The analysis of the first group of systems gives the coupling for the hole transfer process between antenna and donor, while the second group of compounds allows for the estimation of the coupling values associated to the electron transfer between antenna and acceptor. NDI_1-C≡C-NDI_2 is added to the list to decrease the electron tunneling energy barrier height imposed by the phenyl bridge and allow for rotation between the two naphthalene diimides.

To clarify **Table 3.4**, it is worth pointing out the following:

(i) H_{DA} values reported (CTI or CDFT) represent the coupling between the electron or the hole donor and acceptor units, depending on the investigated system.

(ii) In system PTZ-Ph-NDI_1 (L) the HOMO is delocalized over both the PTZ and the phenyl unit. Thus, the latter does no longer constitute a barrier and the McConnel equation can no longer be applied. The $H_{\mathrm{DA}}^{\mathrm{CTI}}$ value is therefore obtained by applying the CTI method, defining PTZ-Ph as the hole acceptor unit, and NDI_1 as the hole donor.

(iii) For all the other cases, no delocalization is observed over the bridge units, that therefore do constitute energy barriers for either hole or electron transfer. The $H_{\mathrm{DA}}^{\mathrm{CTI}}$ values reported in the table are thus obtained by solving equation 3.4 for the $\Delta\varepsilon$ values reported in the table, and the donor-bridge and acceptor-bridge coupling values calculated with the CTI method (not shown).

The CTI and CDFT formalisms give comparable results, despite a different level of theory and environmental constraints applied. Hence the procedure to estimate the tunneling barrier is relatively robust.

Table 3.4. Comparison between the coupling values for hole- and electron-transfer, estimated via CTI and Constrained DFT methods.

	H_{DA}^{CTI}**(meV)**	$\Delta\varepsilon_{hl}$ **(meV)**	H_{DA}^{CDFT} **(meV)**
	Hole transfer Antenna → Donor		
PTZ-Ph-NDI$_1$ (L)	8	-	3
PTZ-Ph-NDI$_1$ (P)	0.3	1000	-
	H_{DA}^{CTI}**(meV)**	$\Delta\varepsilon_{el}$ **(meV)**	H_{DA}^{CDFT} **(meV)**
	Electron Transfer Antenna → Acceptor		
NDI$_1$-Ph-NDI$_2$	0.04	2400	0. 05
NDI$_1$-C≡C-NDI$_2$	23	820	43.5

Electron/hole coupling values H_{DA} and tunneling barriers $\Delta\varepsilon_{hl/el}$ calculated for the subsystems listed in the first column. (L) and (P) indicate the linear or perpendicular configuration of phenothiazine with respect to the phenyl bridge (Ph). CTI Calculations are performed with ADF at the B3LYP/TZP level of theory in DCM (COSMO). The same computational set-up is used to calculate the tunneling-energy gap[62], $\Delta\varepsilon_{hl/el}$. H_{DA}^{CTI} values represent the electron coupling between donor-antenna or antenna-acceptor. The McConnel formalism has been used to calculated the coupling only of those systems for which $\Delta\varepsilon_{hl/el}$ values are reported. Similar hole/electron transfer energy barrier values are obtained using the CDFT approach (not shown). H_{DA}^{CDFT}: coupling values obtained employing the Constrained DFT method implemented in the CPMD package; the CDFT calculations are performed in vacuum, using the BLYP functional and a plane wave cut-off of 70 Ry.

The results shown in **Table 3.4** highlight the large effect of having PTZ linked to the phenyl-bridge in a linear or a perpendicular configuration. The electronic coupling between the hole donor (NDI_1) and the acceptor (PTZ) is reduced by more than one order of magnitude for the perpendicular system.

Binding the PTZ to the phenyl bridge through the amine group of the electron donor, results in loss of conjugation between the two groups. This prevents a strong mixing of the electronic states of the two groups, reduces the electronic coupling and promotes the separation of their energy levels. This results in the bridge imposing a large barrier (1 eV) for the hole-transfering process. On the contrary, conjugation between the PTZ and the bridge is achieved by binding the two in a linear configuration. This allows for strong overlap between the orbitals of the two subunits, resulting into the delocalization, and stabilization, of the supramolecular complex HOMO over both the PTZ and the bridge. Thus, Ph does no longer constitute a barrier for hole transfer; instead it becomes a part of the electron donor. The distance between the hole donor and acceptor is thus reduced, while their electronic coupling is increased.

The use of Ph as bridge unit between NDI_1 and NDI_2 induces a large electron

tunneling barrier (2.4 eV), and reduces the electronic coupling between the two practically to zero. The substitution of the Ph bridge with an acetylene group leads to an increase of the antenna-acceptor electron coupling of four orders of magnitude (**Table 3.4**). This can be explained in terms of the reduced electron donor-acceptor distance imposed by the new bridge, and with the fact that the LUMO of the acetylene is energetically much lower compared to the LUMO of Ph.

By applying this latter change to the structure of system **1_Linear**, we obtain system **1-b_Linear** shown in **Figure 3.5**.

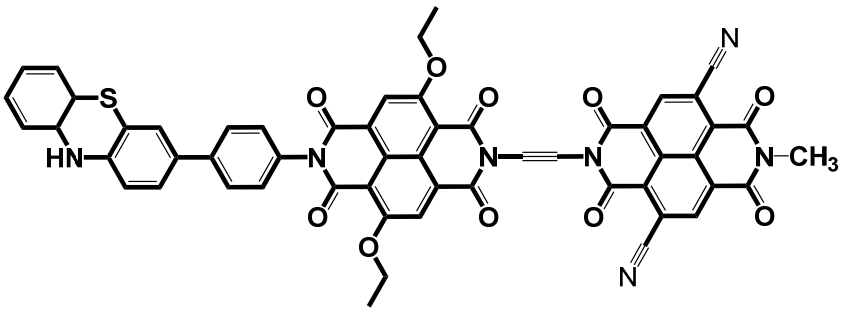

Figure 3.5. Schematic representation of the molecular rectifier **1-b_Linear** optimized for ultrafast formation of the charge separated state S1.

The driving force computed for this triad between S0 and S1, gives $\Delta G = -0.26$ eV, with a reorganization energy λ = 0.7 eV. Instead, the formation of S2 is found to be energetically unfavorable with $\Delta G = 0.1$ eV, and λ = 0.9 eV.

Since the formation of the product state S1 takes place as a concerted hole and electron displacement (see **Scheme 3.2**, left panel), we can reasonably assume that the kinetic bottleneck for this process is represented by the hole transfer from the antenna to the donor. In fact, the electronic coupling calculated between the donor and the antenna in the linear configuration (8 meV, in **Table 3.4**) is weaker than the one between the antenna and the acceptor when connected through an ethyne linker (NDI_1-C≡C-NDI_2, 23 meV in **Table 3.4**). Under this assumption, we can employ equation 3.5 to estimate the rate of formation for S1. By using the values H_{DA} = 0.008 eV, ΔG = -0.26 eV and λ = 0.7 eV, a rate constant k_{ET}= 1.24*10^{12} s^{-1} is obtained, which is similar to the rate of 5*10^{12} s^{-1} experimentally observed for the process of hole transfer between a perylene and a phenothiazine linked through a *p*-phenylene oligomer.

3.4.CONCLUSIONS

With the goal of engineering a molecular triad able to induce a stable charge separated state upon visible light absorption, we design several complexes employing PTZ, NDI_1, and NDI_2 respectively as electron donor, antenna and electron acceptor, using different linkages between these subunits. The investigation of the optical properties performed for each triad reveals a predominant $\pi-\pi^*$ excitation around 500 nm associated with the antenna-localized excited state S0. The relative energetic stability of this initial excited state with respect to the excited states with charge transfer character is found to be dependent on the donor-antenna distance. The separation of these two moieties by means of one phenyl ring appears to be the optimal compromise to ensure a strong driving force for the formation of the fully charge separated state S1 starting from S0 and prevent the occurrence of competing quenching paths for the excitonic state.

It is found that a strong coupling between the donor and antenna is achieved when the PTZ is linked to the phenyl bridge through one of its peripheral aromatic rings. At the same time the ethyne group is shown to provide a strong electronic coupling between the antenna and the acceptor moieties.

Based on these findings, we propose the molecular rectifier PTZ-Ph-NDI_1-C≡C-NDI_2, as a promising triad for photoinduced direct ultrafast charge separation. Recombination of the photoinduced CS state to the ground state is expected to be strongly delayed due to the long distance and large energy barrier between donor and acceptor imposed by the other molecular components. Additionally, in an ensemble where multiple rectifiers are stacked through $\pi-\pi$ interactions, the n-type semiconductor behavior of NDI_2 will have two major advantages: it will further delay charge recombination by delocalizing the electron in the bulk and allow the creation of a p-n junction with a suitable electrode such as silicon. The next steps currently under investigation are a more comprehensive description of the dynamics associated with the ET process and the substitution of the electron donor with a water oxidation catalyst to develop a genuine artificial photosynthesis device[58].

3.5. REFERENCES

(1) Young, K. J.; Martini, L. A.; Milot, R. L.; Snoeberger III, R. C.; Batista, V. S.; Schmuttenmaer, C. A.; Crabtree, R. H.; Brudvig, G. W. Light-Driven Water Oxidation for Solar Fuels. *Coordination Chemistry Reviews* **2012**, *256* (21–22), 2503–2520.

(2) Xiao, D.; Martini, L. A.; Snoeberger, R. C.; Crabtree, R. H.; Batista, V. S. Inverse Design and Synthesis of Acac-Coumarin Anchors for Robust TiO_2 Sensitization. *J. Am. Chem. Soc.* **2011**, *133* (23), 9014–9022.

(3) Negre, C. F. A.; Milot, R. L.; Martini, L. A.; Ding, W.; Crabtree, R. H.; Schmuttenmaer, C. A.; Batista, V. S. Efficiency of Interfacial Electron Transfer from Zn-Porphyrin Dyes into TiO_2 Correlated to the Linker Single Molecule Conductance. *J. Phys. Chem. C* **2013**, *117* (46), 24462–24470.

(4) Martini, L. A.; Moore, G. F.; Milot, R. L.; Cai, L. Z.; Sheehan, S. W.; Schmuttenmaer, C. A.; Brudvig, G. W.; Crabtree, R. H. Modular Assembly of High-Potential Zinc Porphyrin Photosensitizers Attached to TiO_2 with a Series of Anchoring Groups. *J. Phys. Chem. C* **2013**, *117* (28), 14526–14533.

(5) Akimov, A. V.; Neukirch, A. J.; Prezhdo, O. V. Theoretical Insights into Photoinduced Charge Transfer and Catalysis at Oxide Interfaces. *Chem. Rev.* **2013**, *113* (6), 4496–4565.

(6) Yang, W. S.; Noh, J. H.; Jeon, N. J.; Kim, Y. C.; Ryu, S.; Seo, J.; Seok, S. I. SOLAR CELLS. High-Performance Photovoltaic Perovskite Layers Fabricated through Intramolecular Exchange. *Science* **2015**, *348* (6240), 1234–1237.

(7) Jeon, N. J.; Noh, J. H.; Yang, W. S.; Kim, Y. C.; Ryu, S.; Seo, J.; Seok, S. I. Compositional Engineering of Perovskite Materials for High-Performance Solar Cells. *Nature* **2015**, *517* (7535), 476–480.

(8) Moser, C. C.; Keske, J. M.; Warncke, K.; Farid, R. S.; Dutton, P. L. Nature of Biological Electron Transfer. *Nature* **1992**, *355* (6363), 796–802.

(9) Noy, D.; Moser, C. C.; Dutton, P. L. Design and Engineering of Photosynthetic Light-Harvesting and Electron Transfer Using Length, Time, and Energy Scales. *Biochimica et Biophysica Acta (BBA) - Bioenergetics* **2006**, *1757* (2), 90–105.

(10) Allen, J. F. Photosynthesis of ATP—electrons, Proton Pumps, Rotors, and Poise. *Cell* **2002**, *110* (3), 273–276.

(11) Golbeck, J. H. Structure, Function and Organization of the Photosystem I Reaction Center Complex. *Biochimica et Biophysica Acta (BBA) - Reviews on Bioenergetics* **1987**, *895* (3), 167–204.

(12) Gust, D.; Moore, T. A.; Moore, A. L. Solar Fuels via Artificial Photosynthesis. *Acc. Chem. Res.* **2009**, *42* (12), 1890–1898.

(13) Andrea Rozzi, C.; Maria Falke, S.; Spallanzani, N.; Rubio, A.; Molinari, E.; Brida, D.; Maiuri, M.; Cerullo, G.; Schramm, H.; Christoffers, J.; et al. Quantum Coherence Controls the Charge Separation in a Prototypical Artificial Light-Harvesting System. *Nat Commun* **2013**, *4*, 1602.

(14) Yella, A.; Lee, H.-W.; Tsao, H. N.; Yi, C.; Chandiran, A. K.; Nazeeruddin, M. K.; Diau, E. W.-G.; Yeh, C.-Y.; Zakeeruddin, S. M.; Grätzel, M. Porphyrin-Sensitized Solar Cells with Cobalt (II/III)–Based Redox Electrolyte Exceed 12 Percent Efficiency. *Science* **2011**, *334* (6056), 629–634.

(15) Megiatto Jr, J. D.; Méndez-Hernández, D. D.; Tejeda-Ferrari, M. E.; Teillout, A.-L.; Llansola-Portolés, M. J.; Kodis, G.; Poluektov, O. G.; Rajh, T.; Mujica, V.; Groy, T. L.; et al. A Bioinspired Redox Relay That Mimics Radical Interactions of the Tyr–His Pairs of Photosystem II. *Nat Chem* **2014**, *6* (5), 423–428.

(16) Nattestad, A.; Mozer, A. J.; Fischer, M. K. R.; Cheng, Y.-B.; Mishra, A.; Bäuerle, P.; Bach, U. Highly Efficient Photocathodes for Dye-Sensitized Tandem Solar Cells. *Nat Mater* **2010**, *9* (1), 31–35.

(17) Listorti, A.; O'Regan, B.; Durrant, J. R. Electron Transfer Dynamics in Dye-Sensitized Solar Cells. *Chem. Mater.* **2011**, *23* (15), 3381–3399.

(18) Suraru, S.-L.; Würthner, F. Core-Tetrasubstituted Naphthalene Diimides by Stille Cross-Coupling Reactions and Characterization of Their Optical and Redox Properties. *Synthesis* **2009**, *2009* (11), 1841–1845.
(19) Supur, M.; El-Khouly, M. E.; Seok, J. H.; Kay, K.-Y.; Fukuzumi, S. Elongation of Lifetime of the Charge-Separated State of Ferrocene–Naphthalenediimide–[60]Fullerene Triad via Stepwise Electron Transfer. *J. Phys. Chem. A* **2011**, *115* (50), 14430–14437.
(20) Wenger, O. S. Long-Range Electron Transfer in Artificial Systems with d6 and d8 Metal Photosensitizers. *Coordination Chemistry Reviews* **2009**, *253* (9–10), 1439–1457.
(21) Steyrleuthner, R.; Schubert, M.; Howard, I.; Klaumünzer, B.; Schilling, K.; Chen, Z.; Saalfrank, P.; Laquai, F.; Facchetti, A.; Neher, D. Aggregation in a High-Mobility N-Type Low-Bandgap Copolymer with Implications on Semicrystalline Morphology. *J. Am. Chem. Soc.* **2012**, *134* (44), 18303–18317.
(22) Kishore, R. S. K.; Kel, O.; Banerji, N.; Emery, D.; Bollot, G.; Mareda, J.; Gomez-Casado, A.; Jonkheijm, P.; Huskens, J.; Maroni, P.; et al. Ordered and Oriented Supramolecular N/p-Heterojunction Surface Architectures: Completion of the Primary Color Collection. *J. Am. Chem. Soc.* **2009**, *131* (31), 11106–11116.
(23) Sakai, N.; Mareda, J.; Vauthey, E.; Matile, S. Core-Substituted Naphthalenediimides. *Chem. Commun.* **2010**, *46* (24), 4225–4237.
(24) Bhosale, S. V.; Jani, C. H.; Langford, S. J. Chemistry of Naphthalene Diimides. *Chemical Society Reviews* **2008**, *37* (2), 331.
(25) Jones, B. A.; Facchetti, A.; Marks, T. J.; Wasielewski, M. R. Cyanonaphthalene Diimide Semiconductors for Air-Stable, Flexible, and Optically Transparent N-Channel Field-Effect Transistors. *Chem. Mater.* **2007**, *19* (11), 2703–2705.
(26) Gomurashvili, Z.; Crivello, J. V. Phenothiazine Photosensitizers for Onium Salt Photoinitiated Cationic Polymerization. *Journal of Polymer Science Part A: Polymer Chemistry* **2001**, *39* (8), 1187–1197.
(27) Jones, B. A.; Facchetti, A.; Wasielewski, M. R.; Marks, T. J. Tuning Orbital Energetics in Arylene Diimide Semiconductors. Materials Design for Ambient Stability of N-Type Charge Transport. *J. Am. Chem. Soc.* **2007**, *129* (49), 15259–15278.
(28) Guerra, C. F.; Snijders, J. G.; Velde, G. te; Baerends, E. J. Towards an Order-N DFT Method. *Theor Chem Acc* **1998**, *99* (6), 391–403.
(29) Te Velde, G.; Bickelhaupt, F. M.; Baerends, E. J.; Fonseca Guerra, C.; van Gisbergen, S. J. A.; Snijders, J. G.; Ziegler, T. Chemistry with ADF. *Journal of Computational Chemistry* **2001**, *22* (9), 931–967.
(30) Te Velde, G.; Bickelhaupt, F. M.; Baerends, E. J.; Fonseca Guerra, C.; van Gisbergen, S. J. A.; Snijders, J. G.; Ziegler, T. Chemistry with ADF. *J. Comput. Chem.* **2001**, *22* (9), 931–967.
(31) Pye, C. C.; Ziegler, T. An Implementation of the Conductor-like Screening Model of Solvation within the Amsterdam Density Functional Package. *Theor Chem Acc* **1999**, *101* (6), 396–408.
(32) Grimme, S.; Antony, J.; Ehrlich, S.; Krieg, H. A Consistent and Accurate Ab Initio Parametrization of Density Functional Dispersion Correction (DFT-D) for the 94 Elements H-Pu. *The Journal of Chemical Physics* **2010**, *132* (15), 154104–154104 – 19.
(33) Pastore, M.; Fantacci, S.; De Angelis, F. Ab Initio Determination of Ground and Excited State Oxidation Potentials of Organic Chromophores for Dye-Sensitized Solar Cells. *J. Phys. Chem. C* **2010**, *114* (51), 22742–22750.
(34) Wang, T.; Brudvig, G. W.; Batista, V. S. Study of Proton Coupled Electron Transfer in a Biomimetic Dimanganese Water Oxidation Catalyst with Terminal Water Ligands. *J. Chem. Theory Comput.* **2010**, *6* (8), 2395–2401.
(35) Gritsenko, O.; Baerends, E. J. Asymptotic Correction of the Exchange–correlation Kernel of Time-Dependent Density Functional Theory for Long-

Range Charge-Transfer Excitations. *The Journal of Chemical Physics* **2004**, *121* (2), 655–660.
(36) Yanai, T.; Tew, D. P.; Handy, N. C. A New Hybrid Exchange–correlation Functional Using the Coulomb-Attenuating Method (CAM-B3LYP). *Chemical Physics Letters* **2004**, *393* (1–3), 51–57.
(37) Jacquemin, D.; Planchat, A.; Adamo, C.; Mennucci, B. TD-DFT Assessment of Functionals for Optical 0–0 Transitions in Solvated Dyes. *J. Chem. Theory Comput.* **2012**, *8* (7), 2359–2372.
(38) Tawada, Y.; Tsuneda, T.; Yanagisawa, S.; Yanai, T.; Hirao, K. A Long-Range-Corrected Time-Dependent Density Functional Theory. *The Journal of Chemical Physics* **2004**, *120* (18), 8425–8433.
(39) M. J. Frisch, G. W. Trucks, H. B. Schlegel, G. E. Scuseria, M. A. Robb, J. R. Cheeseman, G. Scalmani, V. Barone, B. Mennucci, G. A. Petersson, et al. *Gaussian 09, Revision D.01*; Gaussian, Inc.: Wallingford CT, 2009.
(40) Tomasi, J.; Mennucci, B.; Cammi, R. Quantum Mechanical Continuum Solvation Models. *Chem. Rev.* **2005**, *105* (8), 2999–3093.
(41) Newton, M. D. Quantum Chemical Probes of Electron-Transfer Kinetics: The Nature of Donor-Acceptor Interactions. *Chem. Rev.* **1991**, *91* (5), 767–792.
(42) Senthilkumar, K.; Grozema, F. C.; Bickelhaupt, F. M.; Siebbeles, L. D. A. Charge Transport in Columnar Stacked Triphenylenes: Effects of Conformational Fluctuations on Charge Transfer Integrals and Site Energies. *The Journal of Chemical Physics* **2003**, *119* (18), 9809–9817.
(43) Senthilkumar, K.; Grozema, F. C.; Guerra, C. F.; Bickelhaupt, F. M.; Lewis, F. D.; Berlin, Y. A.; Ratner, M. A.; Siebbeles, L. D. A. Absolute Rates of Hole Transfer in DNA. *J. Am. Chem. Soc.* **2005**, *127* (42), 14894–14903.
(44) Oberhofer, H.; Blumberger, J. Electronic Coupling Matrix Elements from Charge Constrained Density Functional Theory Calculations Using a Plane Wave Basis Set. *The Journal of Chemical Physics* **2010**, *133* (24), 244105–244105 – 10.
(45) Oberhofer, H.; Blumberger, J. Charge Constrained Density Functional Molecular Dynamics for Simulation of Condensed Phase Electron Transfer Reactions. *The Journal of Chemical Physics* **2009**, *131* (6), 064101–064101 – 11.
(46) Wu, Q.; Voorhis, T. V. Extracting Electron Transfer Coupling Elements from Constrained Density Functional Theory. *The Journal of Chemical Physics* **2006**, *125* (16), 164105.
(47) *CPMD, Http://www.cpmd.org/, Copyright IBM Corp 1990-2008, Copyright MPI fürFestkörperforschung Stuttgart 1997-2001*.
(48) Goedecker, S.; Teter, M.; Hutter, J. Separable Dual-Space Gaussian Pseudopotentials. *Phys. Rev. B* **1996**, *54* (3), 1703–1710.
(49) McConnell, H. M. Intramolecular Charge Transfer in Aromatic Free Radicals. *The Journal of Chemical Physics* **1961**, *35* (2), 508–515.
(50) Kishore, R. S. K.; Kel, O.; Banerji, N.; Emery, D.; Bollot, G.; Mareda, J.; Gomez-Casado, A.; Jonkheijm, P.; Huskens, J.; Maroni, P.; et al. Ordered and Oriented Supramolecular N/p-Heterojunction Surface Architectures: Completion of the Primary Color Collection. *J. Am. Chem. Soc.* **2009**, *131* (31), 11106–11116.
(51) Perdew, J. P.; Burke, K.; Ernzerhof, M. Generalized Gradient Approximation Made Simple. *Phys. Rev. Lett.* **1996**, *77* (18), 3865–3868.
(52) Gritsenko, O. V.; Schipper, P. R. T.; Baerends, E. J. Approximation of the Exchange-Correlation Kohn–Sham Potential with a Statistical Average of Different Orbital Model Potentials. *Chemical Physics Letters* **1999**, *302* (3–4), 199–207.
(53) Schipper, P. R. T.; Gritsenko, O. V.; van Gisbergen, S. J. A.; Baerends, E. J. Molecular Calculations of Excitation Energies and (hyper)polarizabilities with a Statistical Average of Orbital Model Exchange-Correlation Potentials. *The Journal of Chemical Physics* **2000**, *112* (3), 1344–1352.
(54) Swart, M.; Ehlers, A. W.; Lammertsma, K. Performance of the OPBE Exchange-Correlation Functional. *Molecular Physics* **2004**, *102* (23-24), 2467–2474.

(55) Reiher, M.; Salomon, O.; Hess, B. A. Reparameterization of Hybrid Functionals Based on Energy Differences of States of Different Multiplicity. *Theor Chem Acc* **2001**, *107* (1), 48–55.
(56) Zhao, Y.; Truhlar, D. The M06 Suite of Density Functionals for Main Group Thermochemistry, Thermochemical Kinetics, Noncovalent Interactions, Excited States, and Transition Elements: Two New Functionals and Systematic Testing of Four M06-Class Functionals and 12 Other Functionals. *Theoretical Chemistry Accounts: Theory, Computation, and Modeling (Theoretica Chimica Acta)* **2008**, *120* (1), 215–241.
(57) Zhao, Y.; Truhlar, D. G. A New Local Density Functional for Main-Group Thermochemistry, Transition Metal Bonding, Thermochemical Kinetics, and Noncovalent Interactions. *The Journal of Chemical Physics* **2006**, *125* (19), 194101–194101 – 18.
(58) Weiss, E. A.; Ahrens, M. J.; Sinks, L. E.; Gusev, A. V.; Ratner, M. A.; Wasielewski, M. R. Making a Molecular Wire: Charge and Spin Transport through Para-Phenylene Oligomers. *J. Am. Chem. Soc.* **2004**, *126* (17), 5577–5584.
(59) Pratik, S. M.; Datta, A. Computational Design of Concomitant Type-I and Type-II Porphyrin Sensitized Solar Cells. *Phys. Chem. Chem. Phys.* **2013**, *15* (42), 18471–18481.
(60) Marcus, R. A. On the Theory of Oxidation-Reduction Reactions Involving Electron Transfer. I. *The Journal of Chemical Physics* **1956**, *24* (5), 966–978.
(61) Hanss, D.; Wenger, O. S. Tunneling Barrier Effects on Photoinduced Charge Transfer through Covalent Rigid Rod-Like Bridges. *Inorg. Chem.* **2009**, *48* (2), 671–680.
(62) Wenger, O. S. How Donor−Bridge−Acceptor Energetics Influence Electron Tunneling Dynamics and Their Distance Dependences. *Acc. Chem. Res.* **2011**, *44* (1), 25–35.

3.6.APPENDIX

Table A3.1. Geometrical parameters of the studied systems optimized in the ground state (B3LYP) and for the excited states of interest (CAM-B3LYP). For system 0 we compare the B3LYP and CAM-B3LYP results for the excited state S0. The geometrical parameters and the atomic labeling used in the table are explained in the schematic representation of the model systems.

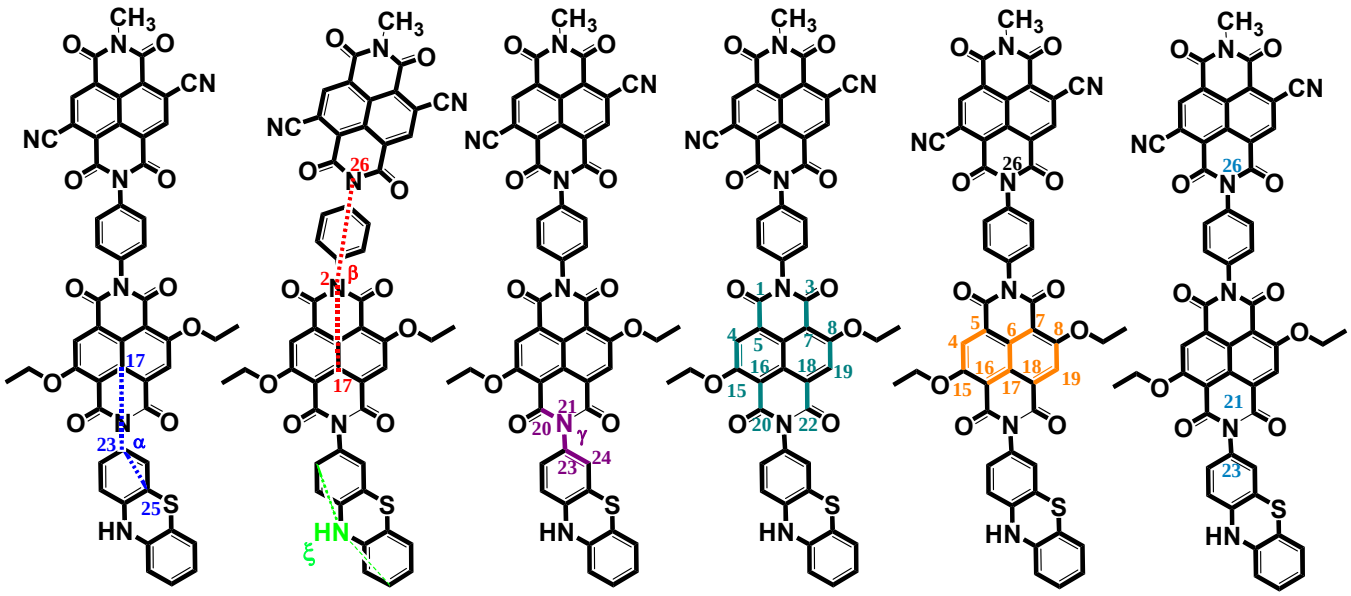

System 0	B3LYP (optimized **GS**)	B3LYP (optimized **S0**)	CAM-B3LYP (optimized **S0**)	CAM-B3LYP (optimized **S1**)	CAM-B3LYP (optimized **S2**)
α (degrees)	149.0	148.3	149.7	150.1	150.7
β (degrees)	179.2	179.4	179.6	179.2	178.6
γ (degrees)	-92.1	-90.4	-97.9	-114.3	-127.0
ξ (degrees)	149.0	146.8	146.8	180.0	180.0
δ 21-23 (Angstrom)	1.47	1.45	1.44	1.43	1.42
δ' 23-26 (Angstrom)	14.19	14.19	14.13	14.12	14.06
1-5	1.48	1.47	1.46	1.48	1.46
3-7	1.48	1.48	1.48	1.48	1.46
4-15	1.42	1.40	1.40	1.42	1.38
8-9	1.42	1.40	1.40	1.42	1.39
15-20	1.48	1.48	1.47	1.47	1.45
18-22	1.49	1.47	1.46	1.48	1.45
SUM (A)	8.77	8.70	8.68	8.75	8.58
AVERAGE (A)	1.46	1.45	1.45	1.46	1.43

System 0	B3LYP (optimized **GS**)	B3LYP (optimized **S0**)	CAM-B3LYP (optimized **S0**)	CAM-B3LYP (optimized **S1**)	CAM-B3LYP (optimized **S2**)
4-5	1.38	1.40	1.39	1.37	1.40
4-15	1.42	1.40	1.40	1.42	1.38
6-7	1.43	1.41	1.40	1.42	1.43
6-17	1.43	1.45	1.45	1.41	1.43
16-17	1.42	1.41	1.40	1.42	1.43
8-19	1.42	1.40	1.40	1.42	1.39
18-19	1.38	1.40	1.39	1.37	1.41
SUM (A)	9.87	9.87	9.82	9.83	9.87
AVERAGE (A)	1.41	1.41	1.40	1.40	1.41

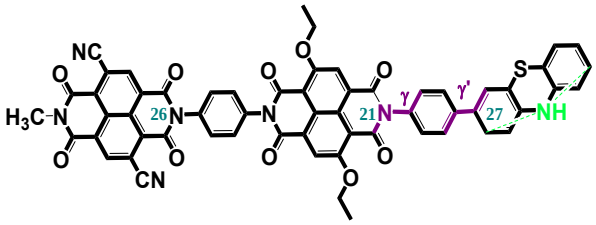

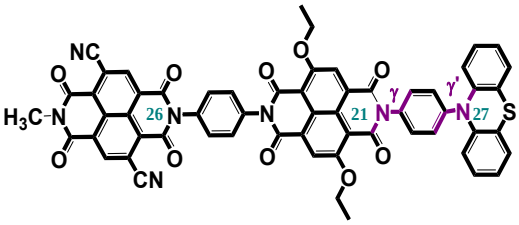

System 1 LINEAR	B3LYP (optimized **GS**)	CAM-B3LYP (optimized **S0**)	CAM-B3LYP (optimized **S1**)	CAM-B3LYP (optimized **S2**)
γ (degrees)	-89.6	-88.6	-91.5	-98.4
γ' (degrees)	34.0	36.4	32.5	26.7
ξ (degrees)	148.9	146.8	177.5	180.0
δ 21-27 (Angstrom)	5.73	5.73	5.71	5.70
δ' 26-27 (Angstrom)	18.35	18.42	18.40	18.33
System 1 PERPENDICULAR	**B3LYP** (optimized **GS**)	**CAM-B3LYP** (optimized **S0**)	**CAM-B3LYP** (optimized **S1**)	**CAM-B3LYP** (optimized **S2**)
γ (degrees)	-90.4	-90.1	-89.0	-90.5
γ' (degrees)	97.8	99.1	89.8	89.8
ξ (degrees)	151.1	149.7	174.0	174.2
δ 21-27 (Angstrom)	5.68	5.65	5.64	5.63
δ' 26-27 (Angstrom)	18.42	18.34	18.33	18.27

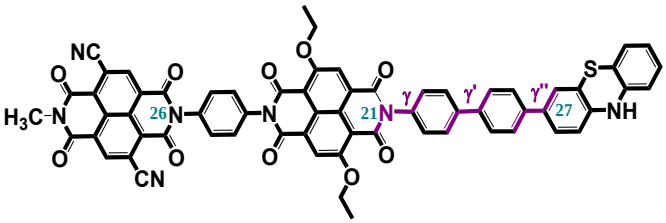

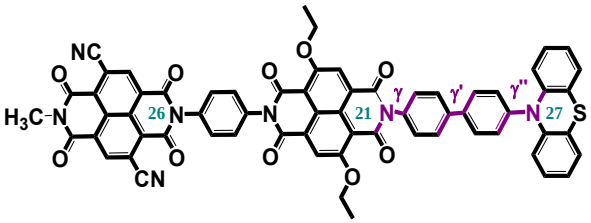

System 2 LINEAR	**B3LYP** (optimized **GS**)	**CAM-B3LYP** (optimized **S0**)	**CAM-B3LYP** (optimized **S1**)	**CAM-B3LYP** (optimized **S2**)
γ (degrees)	-96.2	-90.9	-89.9	-89.1
γ' (degrees)	35.0	36.7	37.0	36.1
γ'' (degrees)	32.1	37.0	33.4	31.5
ξ (degrees)	154.0	148.1	177.6	177.6
δ 21-27 (Angstrom)	10.05	10.05	10.04	10.03
δ' 26-27 (Angstrom)	22.30	22.74	22.73	22.67
System 2 PERPENDICULAR	**B3LYP** (optimized **GS**)	**CAM-B3LYP** (optimized **S0**)	**CAM-B3LYP** (optimized **S1**)	**CAM-B3LYP** (optimized **S2**)
γ (degrees)	-76.8	-94.5	-92.7	-101.3
γ' (degrees)	45.9	37.6	39.6	40.5
γ'' (degrees)	-92.0	-98.5	-90.2	-90.5
ξ (degrees)	149.4	149.0	174.0	174.1
δ 21-27 (Angstrom)	9.98	9.98	9.96	9.96
δ' 26-27 (Angstrom)	22.32	22.66	22.65	22.60